Combustion and Flame 249 (2023) 112625

Contents lists available at ScienceDirect

Combustion and Flame

journal homepage: www.elsevier.com/locate/combustflame

Laminar burning characteristics of coal-based naphtha

Yu Xie[a], An Lu[a,b], Jinzhou Li[a], Junfeng Yang[a,*], Chunhua Zhang[b], Mohamed E. Morsy[a,c]

[a] School of Mechanical Engineering, University of Leeds, Leeds LS2 9JT, United Kingdom
[b] School of Automobile, Chang'an University, Xi'an 710064, PR China
[c] Department of Mechanical Power Engineering, Faculty of Engineering at El-Mattaria, University of Helwan, Cairo 11718, Egypt

ARTICLE INFO

Article history:
Received 29 April 2022
Revised 6 January 2023
Accepted 6 January 2023

Keywords:
Coal-based naphtha
Laminar burning velocity
Flame instability
Surrogate fuel model
PIV

ABSTRACT

Coal-based naphtha is a promising alternative fuel as it fits the standards of energy replacement and is technologically mature, safe, and dependable. However, its laminar combustion characteristics have not been well studied. The laminar burning velocities and Markstein lengths of a kind of coal-based naphtha ($C_{6.97142}H_{15.88244}$) over a range of initial conditions were measured by Particle Imaging Velocimetry (PIV) in spherical explosions. In addition, a 3-component surrogate fuel model (62.4 mol% *n*-C_6H_{14}, 32.5 mol% *i*-C_8H_{18} and 5.1 mol% *i*-C_7H_{16}) based on the Lawrence Livermore National Laboratory (LLNL) gasoline kinetics was proposed according to the detailed hydrocarbon analysis, and then validated against the measured laminar burning velocities. The proposed model performs reasonably well in simulating the laminar burning velocity of coal-based naphtha fuel. Dimensionless parameters including Markstein number, critical Peclet number, critical Karlovitz number and normalized burning velocity, were presented, from which the correlations between thermal diffusion (TD), Darrieus-Landau (DL), thermo-acoustic instabilities and stretch effects were explored. A negative correlation between the combustion intensity deflagration index and Markstein length also demonstrates that a lower stretch effect is favourable to increasing combustion intensity, hence increasing the heat release rate and efficiency of practical combustors.

1. Introduction

The potential of naphtha as a vector for low carbon energy (e.g. less greenhouse gas emissions from fuel processing (petroleum- and coal-based naphtha) or from using renewable fuel sources (bio- and Fischer-Tropsch naphtha)) has only recently been recognised as offering a convincing pathway for the decarbonisation of the transport and energy sectors [1]. Smoothly transitioning to a transport sector that embodies naphtha will require a clear understanding of those applications to which it is well-suited and equally of those to which it is not.

As a by-product of indirect coal liquefaction, coal-based naphtha has the following advantages: (i) naphtha is a light fuel, compared to several other conventional fuels, which helps in improving the mixing and homogeneity of the in-cylinder fresh charge. This also allows for higher compression ratios to be used, and consequently better thermal efficiency [2]; (ii) it has a lower ignition capacity than diesel, but higher than gasoline, avoiding several problems like misfires and poor combustion stability at small loads, and allowing for homogeneous premixing [3]; (iii) naphtha is an intermediate product of the coal refining process, compared to other coal-based diesel and coal-based gasoline, which simplifies the coal refining process to a certain extent (eliminating secondary processes such as reforming and catalytic cracking), reducing greenhouse gas (GHG) emissions and saving costs [4], though coal-to-liquid fuels are generally higher GHG intensity compared to petroleum-based fuels [5]; (iv) coal-based naphtha has no aromatic hydrocarbons and olefins, compared to petroleum-based naphtha. It has a low Research Octane Number (RON 40–60) and contains only marginal aromatic compounds that usually cause secondary pollution to the environment. Previous studies [6,7] show that high olefin contents not only increase the possibility for increased olefin content in exhaust, which increases the potential for ozone production and the tendency for deposit development in engine injectors and intake valves, but also increase the emission of 1,3-butadiene, which are photoreactive and tend to contribute to photochemical smog [8,9]. Aromatic compounds are known to form polycyclic aromatic hydrocarbons (PAHs), which are precursors of soot particles. A number of studies [10–13] have demonstrated a correlation between rising gasoline aromatics content and an increase in particulate matter (PM) emissions. After aromatic hydrocarbons are burned, carcinogenic benzene is

* Corresponding author.
E-mail address: J.Yang@leeds.ac.uk (J. Yang).

https://doi.org/10.1016/j.combustflame.2023.112625

Nomenclature

Ka_{cl}	critical laminar Karlovitz number
k_{st}	deflagration index based on Markstein length (bar/s)
K_{st}	deflagration index (bar·m/s)
$K_{st,0}$	unstretched deflagration index (bar·m/s)
L_b	flame speed Markstein length (mm)
Le	Lewis number
L_u	Markstein length relative to the unburned gases (mm)
Ma	Markstein number
Ma_b	flame burned gas Markstein number
P	pressure (bar)
P_f	peak pressure (bar)
P_i	initial pressure (bar)
Pe_{cl}	critical Peclet number
r_m	mean flame radius based on mass and volume balancing (mm)
r_u	flame cold front radius (mm)
R_0	inner radius of combustion vessel (mm)
R_{PIV}	flame front radius obtained in PIV photography (mm)
S_n	stretched flame speed (m/s)
S_s	unstretched flame speed (m/s)
t	time (s)
T_b	burned temperature (K)
T_i	initial temperature (K)
u_g	maximum outwards gas velocity component normal to the flame front (m/s)
u_l	PIV, unstretched laminar burning velocity, u_n at $\alpha = 0$, Eq. (5) (m/s)
u_{la}	adiabatic density, unstretched laminar burning velocity, Eq. (4) (m/s)
u_n	stretched laminar burning velocity, Eq. (1) (m/s)
u_{nf}	burning velocity at $r_u = 180$ mm (m/s)
u_{tm}	burning velocity obtained from pressure Eq. (8) (m/s)
V_{vessel}	inner volume of combustion vessel (m^3)

Greek symbols

α	flame stretch rate (1/s)
α_{cl}	critical flame stretch rate (1/s)
$\hat{\beta}$	Zeldovich number
γ_u	ratio of specific heat of unburned gas to burned gas
δ	flame thickness (mm)
δ_l	simplistic laminar flame thickness (mm)
ν	unburned gas kinematic viscosity (m^2/s)
ρ	density (kg/m^3)
σ	ratio of unburned gas density to burned gas density
ϕ	equivalence ratio

formed in the tail gas, and carbon deposition in the combustion chamber is increased, resulting in increased tail gas emissions [14]. Overall, coal-based naphtha is a promising alternative fuel for low-carbon transportation energy and power generation.

The ignition properties of petroleum-based naphtha have been well studied experimentally and the corresponding chemical kinetics of combustion have been constructed. Ahmed et al. [15] developed a multi-component surrogate fuel for light naphtha fuel using a multi-variable nonlinear constrained optimization approach. Mitakos et al. [16] investigated the ignition delays of naphtha and primary reference fuels (PRFs) on the rapid compression expansion machine. Alabbad et al. [17] studied the auto-ignition delay times of crude-oil-based naphtha using a shock tube and fast compressor, and proposed a six-component surrogate fuel model (n-pentane, n-heptane, 2-methylhexane, 2,2,4-trimethylpentane, cyclopentane and toluene) and the combustion kinetics to represent the real fuel. Zhong et al. [18] measured ignition delay times for a heavy straight run naphtha fuel (HSRN) and its surrogate blend (a three-component surrogate containing 64.2 mol% iso-pentane, 21.0 mol% n-hexane and 14.8 mol% methylcyclopentane) in a shock tube and rapid compression machine over wide ranges of conditions, indicating that PRFs can be used as an adequate surrogate of HSRN under high-load conditions, whereas multi-component surrogate would be required at low engine loads. Previous work mainly focused on the ignition properties of naphtha due to the fact that naphtha is aimed as a promising fuel for Homogeneous Charge Compression Ignition (HCCI) engine in which the autoignition of reactive mixture dominates the combustion process. Thus, the relevant research on naphtha flame propagation characteristics (e.g. laminar burning velocity, Markstein length) is comparatively marginal. Nevertheless the significance of flame propagation characteristics manifests when the coal-based naphtha is intended to be used (neat or blended with conventional fuels) in gas turbines, or Spark Controlled Compression Ignition (SPCCI) engines or fire safety consideration in chemical refinery plants where flame propagation pattern dominates or exists. Additionally, an understanding of laminar combustion propagation forms a necessary pre-requisite to an understanding of turbulent flames, which is essential to many practical combustion applications. Moreover, the existing kinetic models [17,18] of the naphtha have been developed mainly for petroleum-based naphtha. Since coal-based naphtha has completely different hydrocarbon compositions compared to petroleum-based naphtha, it is necessary to study the laminar flame properties of coal-based naphtha, and to develop its surrogate fuel model and chemical kinetics of combustion.

The *in-situ* burning velocity measurement based on the time-resolved PIV technique is used in this study. The PIV method is able to measure the local unburned gas velocity, u_g, ahead of the flame directly by tracking the instantaneous position of seeding particles. The digital images recording the scattered light from the particles can be proceeded to extract the flame contours and flame speeds, S_n. Therefore, the burning velocity of flames can be derived directly using $u_n = S_n - u_g$ without assuming that the burned gas density at zero stretch rate is that of an adiabatic flame under equilibrium conditions. It has been used to measure the laminar burning velocity of hydrogen, methane, propane, ethanol, n-butanol and iso-octane mixtures with air [19–22]. This technique has been employed in the present work for investigating the laminar flame characteristics of coal-based naphtha.

The objectives of this research are: (i) developing a surrogate fuel model based on the fuel composition analysis and the existing gasoline combustion kinetics; (ii) measuring the laminar burning velocity of coal-based naphtha using PIV technique and validating the established surrogate fuel model; (iii) investigating its laminar combustion characteristics using a spherical flame configuration including deflagration index, K_{st}, unstretched flame speed, S_s, unstretched laminar burning velocity, u_l, burned gas Markstein number, Ma_b, stretch rates at the onset of flame instabilities, α_{cl}, critical Peclet number, Pe_{cl}, and critical Karlovitz number, Ka_{cl}. (iv) defining the stable and unstable regime using dimensionless groups (Pe_{cl}, Ka_{cl} and Ma_b) and studying the complex evolution of thermo-acoustic instability of naphtha-air mixtures.

2. Composition of coal-based naphtha and surrogate model

The coal-based naphtha, provided by China National Energy Group Ningxia Coal Industry Co. Ltd., was used in the present

Table 1
Properties of coal-based naphtha.

Properties	Coal-based naphtha
Research octane number (RON)	54
Lower heating value (MJ/kg)	45.73
Density at 20°C (g/cm^3)	0.67
Kinematic viscosity at 20°C (mm^2/s)	0.56
Sulfur content (mg/kg)	<1
Nitrogen content (mg/kg)	<1
Water content (mg/kg)	356

work. The important thermo-physical properties of such fuel, e.g. heating value, density and viscosity, are listed in Table 1 [2].

The Gas Chromatography-Detailed Hydrocarbon Analysis (GCDHA) summarized in Table 2 shows that the major constituents in the coal-based naphtha sample are C_3-C_{10} n-paraffins (20.18 wt%), iso-paraffins (75.64 wt%) and naphthenes (3.78 wt%). However, coal-based naphtha has no olefins and aromatics. Clearly, coal-based naphtha has different properties and compositions compared to petroleum-based naphtha [17,18] which contains a certain amount (10–15 wt%) of cyclic hydrocarbons.

The chemical formula of coal-based naphtha ($C_{6.97142}H_{15.88244}$) and H/C ratio (2.278) were determined by taking the sum of the property of each component multiplied by its molar fraction calculated from the mass fraction in Table 2. In addition, the present work proposes a three-component surrogate model (n-hexane, *n*-C_6H_{14}: iso-octane, *i*-C_8H_{18}: iso-heptane, *i*-C_7H_{16} 62.4:32.5:5.1 by mol%) for the coal-based naphtha. The substitute components of this surrogate model were selected according to the method reported by Knop et al. [23] to match the RON and H/C ratio. A comparison of coal-based naphtha and its surrogate model is given in Table 3. Moreover, the combustion kinetics of substituent components (n-hexane, iso-octane and iso-heptane) have been constructed and embedded in LLNL gasoline surrogate combustion kinetics [24]. Therefore, they were adopted here for the 3-component coal-based naphtha surrogate model. This surrogate model was later validated against the laminar burning velocity measured in the Leeds MK-II combustion vessel.

3. Experimental apparatus

A 380-mm-diameter spherical stainless-steel vessel with a total internal volume of 0.030372 m^3 capable of withstanding initial pressure (P_i) of up to 15 bar and initial temperature (T_i) of up to 600 K was used, with wide optical access through three pairs of orthogonal windows (150-mm-diameter). The vessel was equipped with four electric-motor-driven fans that were primarily employed to guarantee that the reactants were well mixed before ignition. To achieve the criteria for evaporation of liquid fuel, two electric heaters (2 kW) were attached to the inner wall of the bomb to warm the vessel and air-fuel mixture. A sheathed chromel-alumel thermocouple was used to monitor the gas temperature. A Kistler pressure transducer was used to detect pressure during an explosion. A 12 V transistorized automobile ignition coil was employed to supply a central spark plug with the lowest ignition energy. More details of the auxiliary can be found in [25].

A dual pulse Nd:YAG laser (Photonics Industries DM60–532-DH model) with a wavelength of 532 nm and an adopted frequency of 5 kHz was used in conjunction with a series of optical devices to create a thin laser sheet in the centre of the combustion chamber. The olive oil droplets ($< 1\ \mu m$ diameter) with a boiling temperature of 570 K were introduced into the fluid as tracer particles, which travel in lockstep with the local velocity. Due to the evaporation of the seeding particles, the burnt gas appears black. The greyish-white region outside of the flame was illuminated by the Mie scattering of seeding particles irradiated by the laser sheet. More details of the PIV setup and processing procedures can be found in [22]. A perpendicularly positioned Ultrahigh-Speed Phantom v2512 camera records a 12-bit picture pair of 768 × 768 pixels at a frame rate of 5000. The pixel size is calculated as 0.222 mm/pixel. Measurements of coal-based naphtha-air mixture were made at the initial condition of $T_i = 360$ K, $P_i = 1, 3, 5$ bar in spherical explosion flames over a wide range of equivalence ratios ($\phi = 0.8$–1.5). For the sake of validation and comparison, Measurements of iso-octane and n-heptane-air mixtures were carried out at the initial condition of $T_i = 360$ K, $P_i = 5$ bar and $\phi = 0.8$–1.5.

4. Data processing method

The raw PIV images can be post-processed using Dantec Dyamicstudio 5.1 [26]. The procedure for extracting the flame contour and unburnt gas velocity is given in Fig. 1 [25]. Following the capturing of pictures of the seeding particles by the PIV system, an assessment was carried out to determine the velocities present. An adaptive algorithm known as the Adaptive PIV approach was employed within the Dantec Dyamicstudio 5.1. This was an iterative and automated technique for computing velocity vectors based on seeding particle density and flow gradients. The first step in this process was to divide the recorded image pair into geographically matching interrogation areas, or IAs. The direction, shape, and size of individual IAs were changed several times to match local seeding densities and velocity gradients.

For an outwardly propagating spherical flame, the stretched laminar burning velocity, u_n, is given directly by the stretched flame speed (S_n) and the fresh gas velocity at the entrance of the flame front (u_g) [22]:

$$u_n = S_n - u_g \tag{1}$$

where the stretched flame speed, S_n is calculated from the derivative time of the flame cold front radius, r_u; r_u is calculated from the front radius defined in PIV photography (R_{PIV}), shown in [22]. Using an image-balanced tool in Dantec software, the flame edge was identified from the images by initially increasing the low-level brightness. Light sheet non-uniformities impact the output of other analytic algorithms, and this utility corrects them. The burned and unburned gas were distinguished using the binarization tool in MATLAB R2019a [27]. Then, in binary pictures, the 'imfill' function was used to fill gaps and incoherent areas. The 'bwperim' function was used to find the perimeter of flame contour edges in a binary picture. A low pass filter was used to smooth the observed flame edges and remove any noise. The best fit circle to the flame edge and the matching flame radius, r_u, were then determined using the least squares technique. The value of u_g (maximum outwards gas velocity component normal to the flame) can be obtained from the gas vectors ahead of the flame surface, which is also the rate of entrainment of cold unburned gas by the flame front. The details of obtaining u_g can be found in [21,22].

The total stretch rate at the cold front of the flame is:

$$\alpha = \frac{1}{A}\frac{dA}{dt} = \frac{2}{r_u}\frac{dr_u}{dt} = \frac{2}{r_u}S_n \tag{2}$$

where A is the laminar flame surface area. The linear extrapolation model is adopted to delineate the relationship between S_n and α:

$$S_s - S_n = L_b\alpha \tag{3}$$

Here S_s is the flame speed at zero stretch rate. The equation yields values of burned gas Markstein length of flame speed, L_b, which can be normalised with respect to the flame thickness to yield Markstein number Ma_b. The unstretched laminar burning velocity using the mass conservation is calculated by:

$$u_{la} = S_s\frac{\rho_b}{\rho_u} \tag{4}$$

Table 2
The GCDHA results of coal-based naphtha (by mass percent).

Carbon	n-Paraffins	Isoparaffins	Olefins	Naphthenes	Aromatics	Total
C3:	0.009					0.009
C4:	0.567	0.631				1.198
C5:	3.467	7.348		0.007		10.822
C6:	4.993	15.208		0.253		20.454
C7:	4.728	17.188		0.536		22.452
C8:	4.393	17.517		1.884		23.794
C9:	1.992	16.044		1.104		19.140
C10:	0.033	1.705				1.738
Total	20.182	75.641	0.000	3.784	0.000	99.607

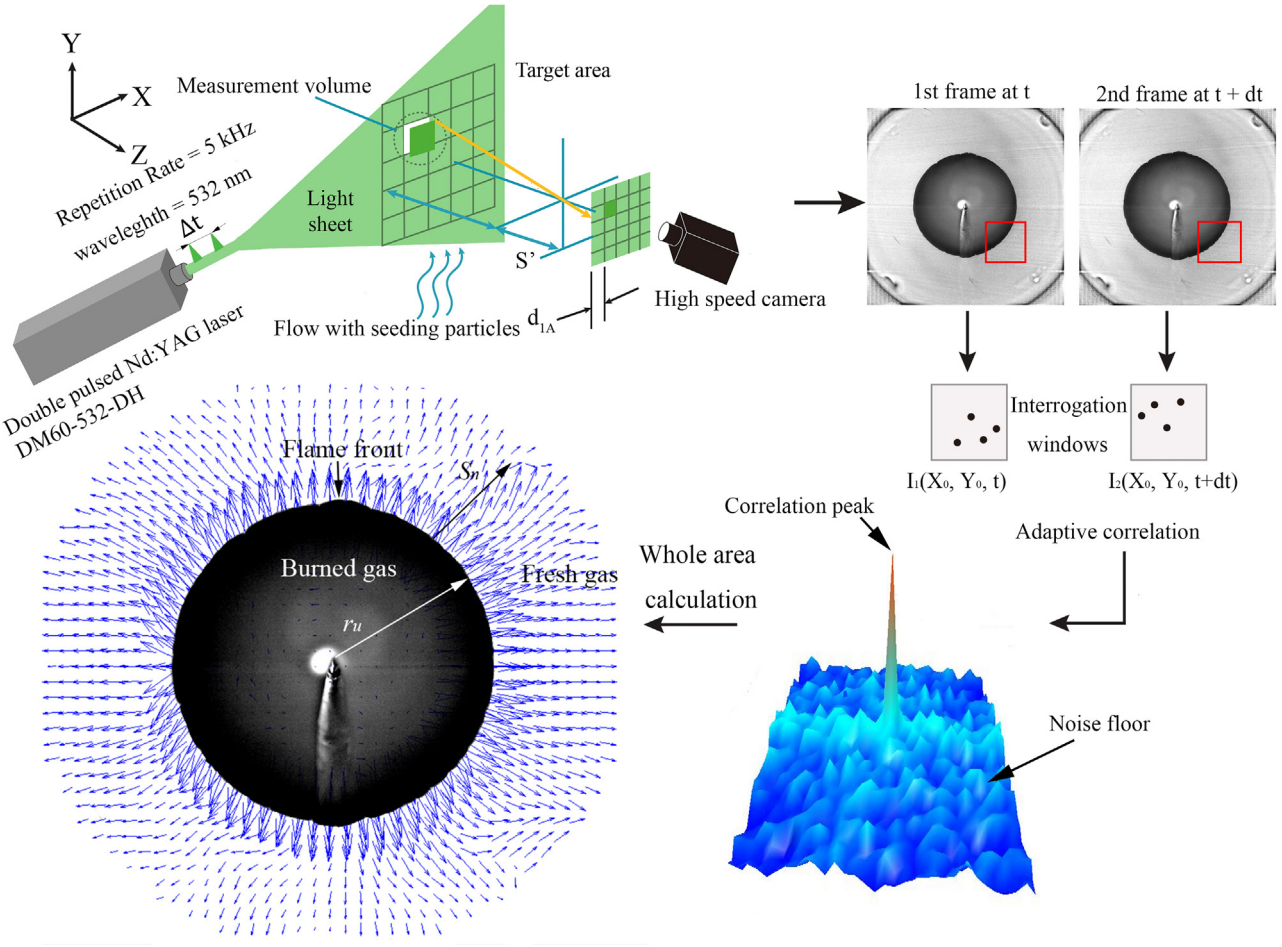

Fig. 1. 2D field calculation of PIV flame image and gas vectors using adaptive correlation [25].

Table 3
Comparison of coal-based naphtha and its surrogate.

	Coal-based naphtha	3-component surrogate
Average chemical formula	$C_{6.97142}H_{15.88244}$	$C_{6.701}H_{15.402}$
RON	54	54
H/C ratio	2.278	2.298
Average molecular weight	99.742	95.814
n-Paraffins (mole%)	20.182	62.4
Isoparaffins (mole%)	75.641	37.6
Olefins (mole%)	0.000	0.000
Naphthenes (mole%)	3.784	0.000
Aromatics (mole%)	0.000	0.000

where ρ_b is burned gas density (kg/m^3), ρ_u is unburned gas density (kg/m^3).

Similarly, using Eq. (1), the unstretched laminar velocity, u_l, can be also calculated as follows:

$$u_n = u_l - L_u\alpha \tag{5}$$

where L_u is the Markstein length relative to the unburned gases (i.e. fresh gases).

According to the nonlinear asymptotic theory [28], the nonlinear extrapolation method [29–31] is chosen for comparison with the linear extrapolation approach:

$$\left(\frac{S_n}{S_s}\right)^2 \ln\left(\left(\frac{S_n}{S_s}\right)^2\right) = -2\frac{L_b\alpha}{S_s} \tag{6}$$

The pressure record is used to obtain the volume-equivalent radius, r_m, of the flame according to [32]:

$$r_m = R_0\left\{1 - \left(\frac{P_i}{P}\right)^{1/\gamma_u}\left[\frac{P_f - P}{P_f - P_i}\right]\right\}^{1/3} \tag{7}$$

where R_0 is the inner radius of vessel, P_i and P_f are the initial and peak pressures, and γ_u is the ratio of specific heat of unburned gas to burned gas.

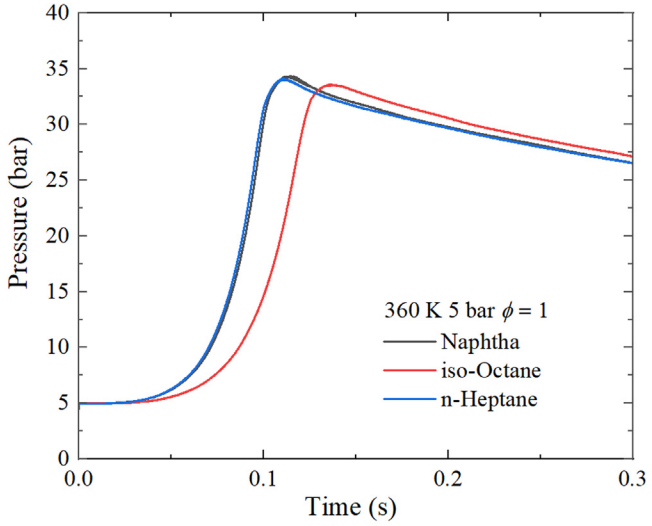

Fig. 2. Evolutions of the pressure inside the vessel during the combustion of coal-based naphtha, iso-octane and n-heptane-air mixtures at $P_i = 5$ bar, $T_i = 360$ K and $\phi = 1.0$.

The appropriate u_{tm} based on the pressure can be acquired from the mass fractional burning rate, and the approximate burning velocity is calculated by [32]:

$$u_{tm} = \left(\frac{P_i}{P}\right)^{1/\gamma_u}\left\{1 - \left(\frac{P_i}{P}\right)^{1/\gamma_u}\left[\frac{P_f - P}{P_f - P_i}\right]\right\}^{-2/3}\frac{R_0}{3\left(P_f - P_i\right)}\frac{dP}{dt} \quad (8)$$

A key parameter is the critical flame radius, r_{cl}, the flame radius at which the cellular flame structure becomes apparent. The appropriate dimensionless radius is the critical Peclet number, Pe_{cl}, as [33]:

$$Pe_{cl} = \frac{r_{cl}}{\delta_l} \quad (9)$$

where $\delta_l \cong \nu/u_l$ is an approximate guide to the flame thickness [34]. ν is the unburnt gas kinematic viscosity. The procedures for defining the onset of instability and r_{cl} are described in [31].

Pe_{cl} does show the dimensionless critical radius of its commencement, but it does not represent the underlying cause of cellularity. Since the flame is stabilised by the stretch, a laminar critical Karlovitz number, Ka_{cl}, expressed on the basis of the critical total flame stretch rate, α_{cl}, is presented to show the fundamental characteristics of the flame instability rather than Pe_{cl}. It is readily shown that [33] and Appendix 1:

$$Ka_{cl} = (2\sigma/Pe_{cl})[1 + (2Ma_b/Pe_{cl})]^{-1} \quad (10)$$

where σ is the ratio of unburned gas density to burned gas density. Qaseq code [35] is used to retrieve the aforementioned parameters, including ν, σ, and further other parameters can be obtained by PIV method.

5. Results and discussions

5.1. Combustion pressure

Figure 2 illustrates the pressure traces for coal-based naphtha, iso-octane, and n-heptane-air mixtures within 0.3 s, demonstrating that the complete volume of the fresh gases is burned in a substantially shorter period. The influence of mixture strength (ϕ) and initial pressure (P_i) on the evolution of pressure inside the spherical vessel is also significant. The consumption of n-heptane is substantially faster than that of iso-octane, implying that the n-heptane-air mixture burns more quickly. The pressure trace of coal-based naphtha lies somewhere between typical iso-octane and n-heptane-air combustion, and it is fairly close to n-heptane. Despite the differences in time to attain peak pressure, the maximum pressure of the three fuels is nearly close.

Figure 3 shows different pressure traces of coal-based naphtha-air mixtures over a wide range of initial conditions. The time the combustion mixture takes to attain maximum pressure decreases from the lean mixture to the rich mixture, which is owing to higher burning rates and unstable flames under $P_i = 3$, 5 bar. The formations of high-frequency pressure oscillations can be seen in the rich mixtures (e.g. $\phi = 1.2$–1.5) and under the elevated pressures (e.g. $P_i = 3$, 5 bar). Moreover, the larger P_i is, the more pressure traces oscillate. At peak pressure, the oscillations exhibited a dominating frequency of 1.5 kHz, which roughly matched the transit duration of an acoustic wave over the diameter [36]. The oscillations appeared to be caused by a rapid increase in the burning rate approximately 0.05–0.1 s after igniting the mixtures. When pressure gradients are oriented orthogonally to the high-density gradients at the flame surface, Taylor instabilities can wrinkle the flame surface extensively, and vorticity is generated through the baroclinic term, $\nabla(1/\rho) \times \nabla P$, [36]. Furthermore, as the combustion energy is released, it feeds the positive phase of a pressure wave, and consequently Rayleigh instability arises. The Rayleigh and Taylor thermo-acoustic instabilities are frequently combined in practice.

Pressure oscillations and thermo-acoustic instabilities can be triggered by a sufficiently high rate of change in the heat release. The deflagration index (combustion intensity), K_{st}, is determined from the evolution of the pressure inside the vessel as a function of time, as shown in the following equation [37]:

$$K_{st} = \left(\frac{dP}{dt}\right)_{\max}\left(V_{vessel}\right)^{1/3} \quad (11)$$

The moderate growth of K_{st} can be clearly found from $\phi = 0.8$ to 1.2 in Fig. 4, indicating relatively stable and nonviolent flames. However, a sudden increase in K_{st} suggests an increase in combustion intensity, especially for rich mixtures ($\phi = 1.2$ to 1.5). Such mixtures are associated with greater instability in heavy hydrocarbon fuels (e.g. iso-octane and n-heptane), which can also be present in coal-based naphtha.

5.2. Laminar burning velocity

Mie-scattering images at lean ($\phi = 0.8$), stoichiometric ($\phi = 1.0$) and rich ($\phi = 1.2$) mixture and at 0.1 MPa, 0.3 MPa and 0.5 MPa are shown in Fig. 5. At high pressure, some cracks propagate across the flame surface, causing subsequent cellular flames, which are more obvious in the rich mixture. The stretched flame speed S_n can be calculated from the derivative time of the flame radius, r_u.

Figure 6 presents the raw pictures of flame Mie scattering (a) and the gas-related velocity vector (b) of one typical experiment, with the magnitude of the velocity vectors colored in. The continuous expansion of the flame front pushes the unburned gases outwardly ahead of the flame contour. As mentioned in Section 4, the stretched burning velocity u_n can be obtained by $S_n - u_g$ (Eq. (1)).

Variations of unstretched flame speeds (S_s) using linear and nonlinear methods of naphtha-air, iso-octane-air and n-heptane mixtures are plotted against the equivalence ratios in Fig. 7(a). In addition, comparisons with previous data using Schlieren photography and the same combustion chamber [38] are presented. The unstretched flame speeds of the naphtha flames are higher than those of iso-octane flames and lower than those of n-heptane flames. The linear and nonlinear methods present close results, but those from the former are slightly higher than those from the latter, which is consistent with [39,40].

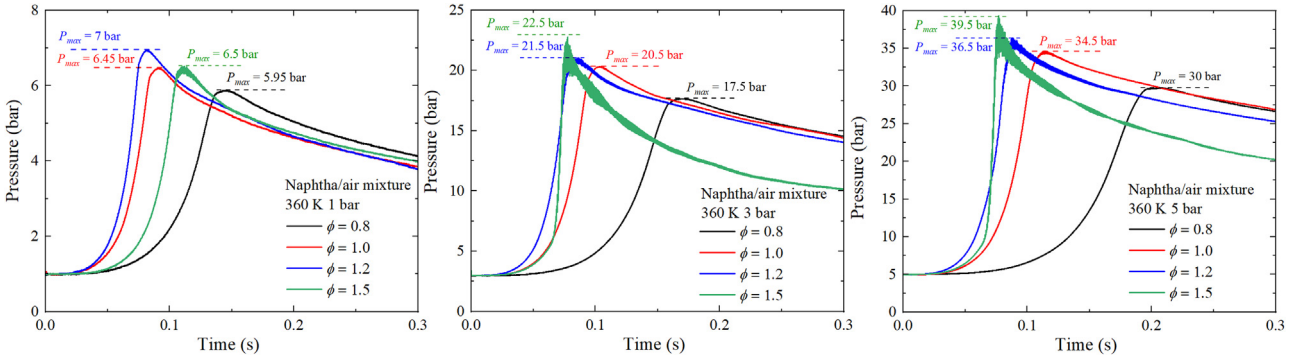

Fig. 3. Evolutions of the pressure inside the vessel during the combustion of coal-based naphtha-air mixtures initially at P_i =1, 3, 5 bar, T_i = 360 K and ϕ = 0.8, 1.0, 1.2, 1.5.

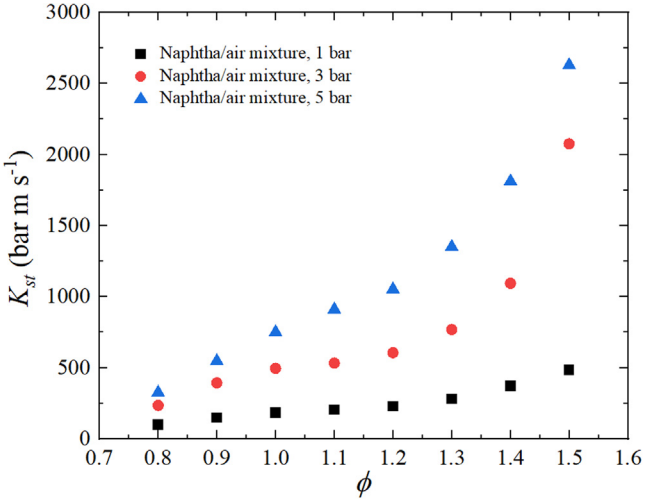

Fig. 4. Variations of deflagration index, K_{st}, for coal-based naphtha-air mixtures at P_i =1, 3, 5 bar, T_i = 360 K.

As previously stated, the stretched flame speed can be estimated as a function of the stretch rate using the burned gas Markstein length L_b. The burned gas Markstein lengths L_b using linear and nonlinear fitting methods are plotted in Fig. 8 at various conditions. Comparison between linear and nonlinear methods shows that burned gas Markstein lengths evaluated using the linear extrapolation are overestimated, especially for the lean conditions. Consequently, the corresponding unstretched flame speeds are exaggerated as well. This is in accordance with [21]. At various equivalence ratios of the fuel mixtures, the influence of pressure on L_b can be readily seen. L_b falls closer to 0 and even less than 0 as the pressure and equivalence ratio increase, showing that the effects of stretch rate on flame stability decrease. Thermo-acoustic instability destabilizes this rich mixture as the equivalence ratio rises. Because the rich fuel-air mixture employed in this work contains heavy hydrocarbons, which have a reduced diffusivity of fuel species compared to the copious oxygen and nitrogen species, this behavior is obtained by lowering the Lewis number of the mixture [41]. However, increasing the pressure enhances hydrodynamic (Darrieus-Landau) instabilities, owing to a considerable decrease in flame thickness [42]. The values of L_b of naphtha-air mixtures are between iso-octane and n-heptane-air mixtures, similar to the distribution of laminar velocity.

Since the difference in S_s between linear and nonlinear methods is small, the conventional linear extrapolation method is adopted to derive the unstretched laminar burning velocity. The unstretched laminar burning velocities of naphtha-air mixtures at various conditions, as determined from Figs. 7 and 8 and using Eqs. (1)-(5), are shown in Fig. 9. Comparisons with previous Schlieren results at 1 bar [38] and current PIV experimental results at 5 bar of iso-octane and n-heptane-air mixtures are also shown for clarity. The patterns of unstretched laminar burning velocities throughout a large range of equivalence ratios are very similar. With a maximum discrepancy of 5% and a mean difference of 3% below the u_l values, the u_{la} values are understated at 1 bar. However, the mean difference at 3 and 5 bars is only around 1%. The difference can be attributed to the burned gas density estimation (computed for burned gases at chemical equilibrium for adiabatic

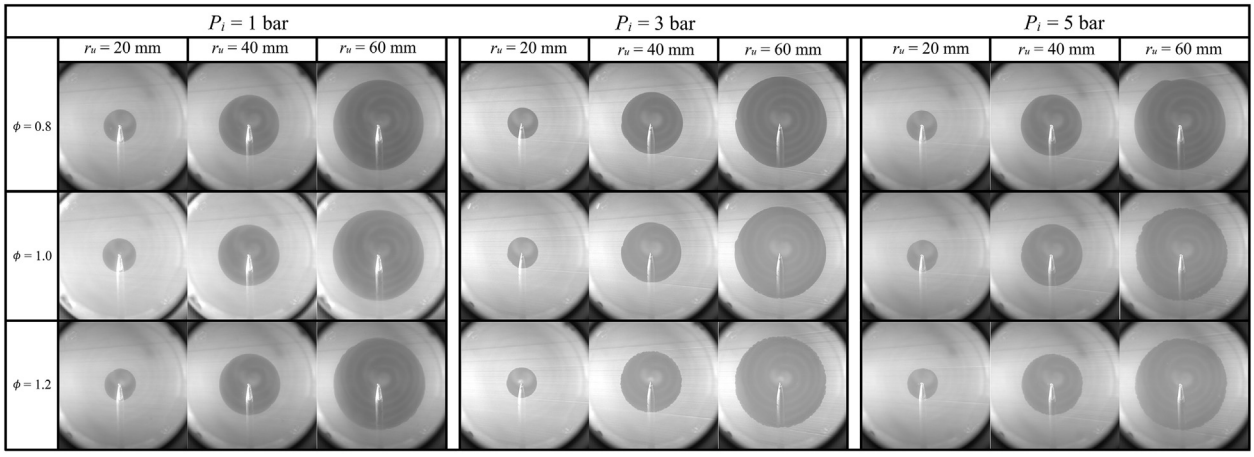

Fig. 5. Development of raw Mie-scattering naphtha-air laminar flames, ϕ = 0.8, 1.0, 1.2, at 1, 3, 5 bar and 360 K, from r_u = 20 to 60 mm.

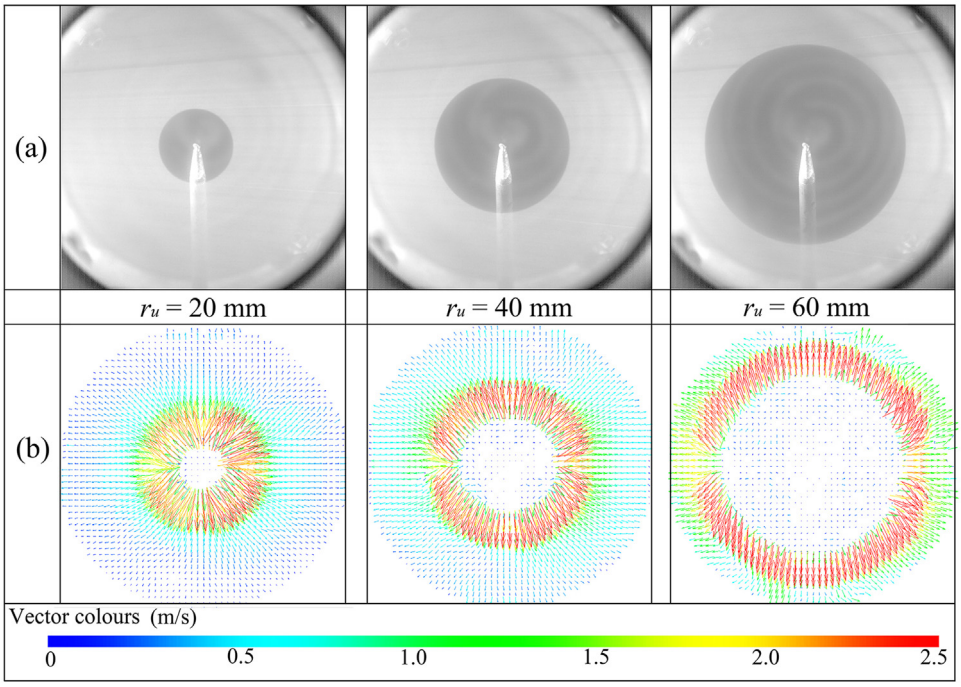

Fig. 6. Development of naphtha-air laminar flame, ϕ =1.0 at 1 bar and 360 K, from r_u = 20 to 60 mm. (a) Raw images, and (b) Vector maps.

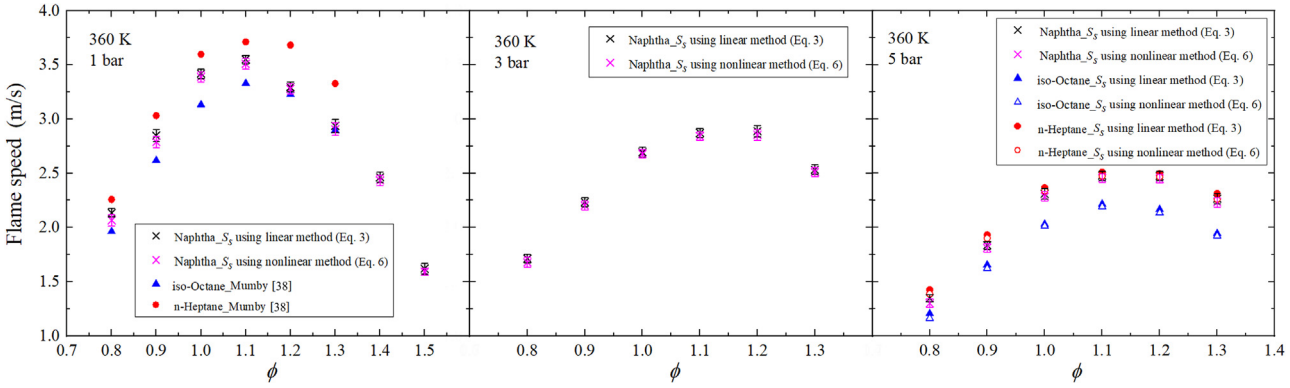

Fig. 7. Unstretched flame speeds of naphtha-air, iso-octane-air and n-heptane mixtures against ϕ. Error bands are for experiments.

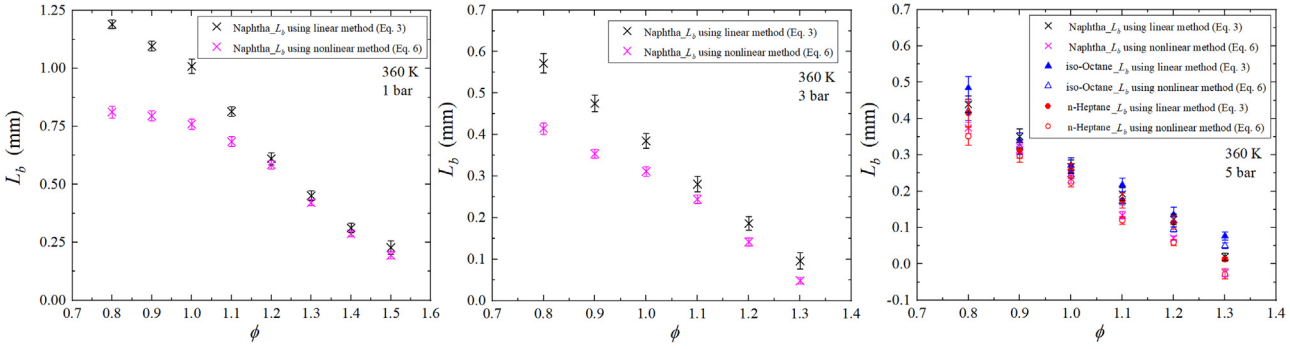

Fig. 8. Experimental values of L_b against ϕ. Error bands are for experiments.

combustion). It takes longer to burn gas at atmospheric pressure than at high pressure to reach chemical equilibrium [21]. Other factors that might impact the outcome include ignition [43], flow confinement [44,45], and radiation [46].

Furthermore, increasing pressure reduces the unstretched laminar burning velocities of naphtha-air mixtures. The proposed 3-component surrogate fuel model mentioned in section 2 was employed here to predict the freely propagation laminar flame using Chemkin-Pro software ver.19.2 [47]. The predicted results are plotted along with the measured data in Fig. 9. Overall, the surrogate fuel model slightly over-predicted the laminar burning velocity at atmospheric pressure. On the other hand, under the elevated pres-

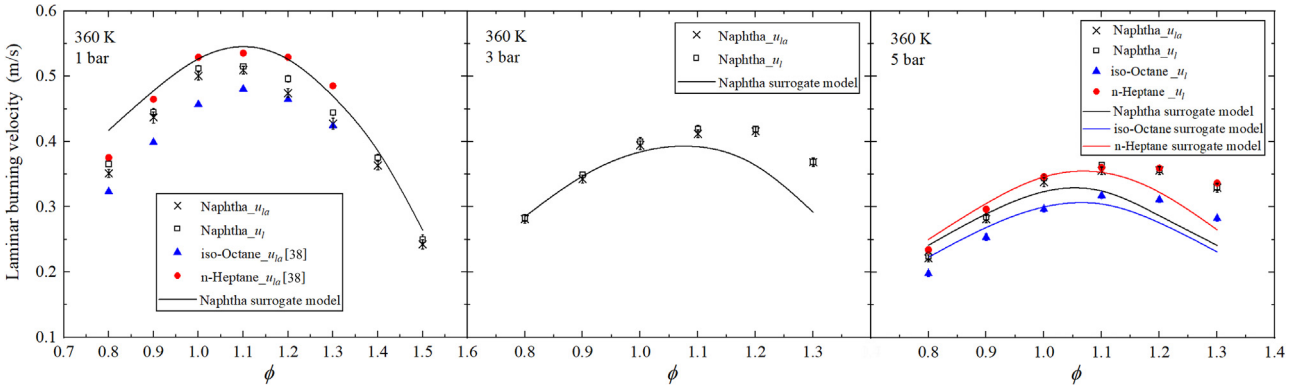

Fig. 9. Unstretched laminar burning velocities of coal-based naphtha, iso-octane and n-heptane-air flames at T_i = 360 K, P_i =1, 3, 5 bar. Error bands are for experiments.

sures, the 3-component surrogate model gave a reasonable prediction under lean and stoichiometric conditions, while falling slightly below the experimental results under rich conditions, which can also be found for the laminar burning velocity of iso-octane and n-heptane at 5 bar. This failure of predictions in rich conditions is a recurrent issue [48,49]. This may be attributed to that flame speed is most sensitive to the formation and destruction of allyl (C_3H_5), of which uncertainty in the C_3H_5 chemistry is much larger than the uncertainty in the hydrogen and CO chemistry [49]. In addition, experimental rate constant data involving the C_3H_5 radical are very limited, and the current reaction rates and pathways in LLNL gasoline surrogate combustion kinetics [24] involving C_3H_5 need to be modified further to improve flame-speed predictions.

Additionally, other factors resulting in a difference could be the missing naphthenes components in the surrogate fuel model. Although the proportion of naphthenes (mainly methyl-cyclopentane and methyl-cyclohexane) is small (3.784 wt%), the bond dissociation energy of cyclic naphthenes is lower because of the ring strain compared to the normal alkanes. Since the bond strengths of napthenes are weaker, more bond breaking produces more radicals, e.g. O, H and OH in the flame and influences the flame speed. However, the elevated pressure not only increases the rate-limiting reaction rate (Termination reaction, e.g. H+O2 +M -> HO2 + M, rate ↑ as pressure ↑) in the flame but also reduces the amount of H, O, and OH radicals in the flame, so as to restrain the propagation of the flame. The addition of naphthene will ensure a better prediction on laminar burning velocity using the present surrogate model.

At atmospheric pressure, due to the low initial pressure, the presence of naphthenes will slow down the burning velocities of coal-based naphtha, so the simulation results are slightly higher than the actual experimental results of coal-based naphtha. With the increase of the initial pressure, the influence of naphthenes decreases, and the experimental results are closer to the simulation results. Therefore, naphthenes need to be considered as the main constituent component of the surrogate model (e.g. 4-component model) to better predict the pressure effect on laminar burning velocity.

5.3. Flame instability assessment of coal-based naphtha

Based on $\delta_l \approx \nu/u_l$, the flame thickness of naphtha, iso-octane, and n-heptane-air mixtures are presented in Fig. 10. At P_i = 5 bar, naphtha, iso-octane, and n-heptane-air mixtures have flame thicknesses that are quite near to each other, with the naphtha-air mixture being somewhere in the middle.

Cellular instability of premixed flames is commonly observed in combustion fundamentals, which is controlled by thermal diffusion (TD) and hydrodynamic, Darrieus–Landau (DL) instabilities. Fig. 11

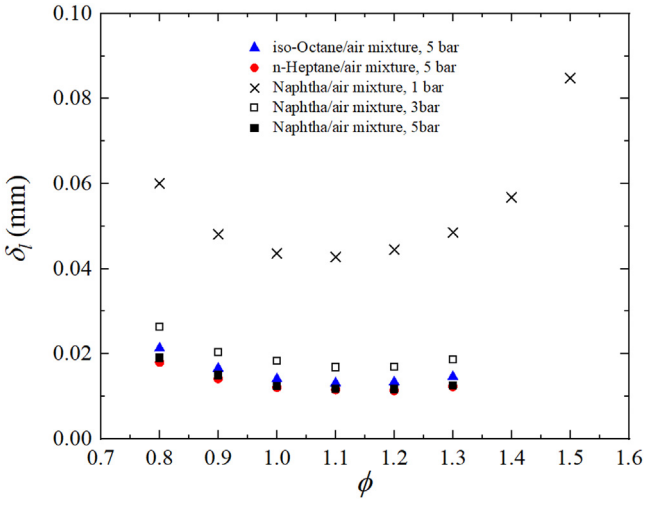

Fig. 10. Variations of flame thickness on different equivalence ratios for coal-based naphtha, iso-octane and n-heptane-air mixtures at T_i = 360 K.

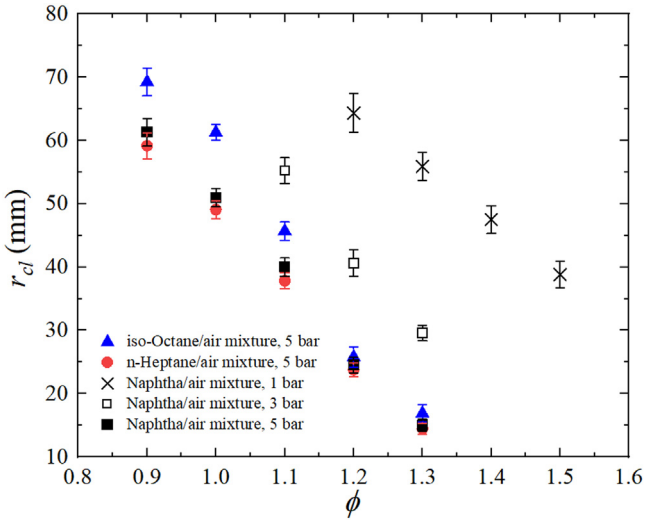

Fig. 11. Experimental values of critical radii for coal-based, iso-octane and n-heptane-air mixtures at P_i = 1, 3, 5 bar, T_i = 360 K. Error bands are for experiments.

shows the experimental values of r_{cl} against ϕ for various mixtures. As P_i and ϕ rises, r_{cl} drops in coal-based naphtha, iso-octane, and n-heptane-air flames, suggesting a more unstable flame.

Because of the increased flame surface area, flame fronts that experience cellular instabilities have a higher burning rate. In

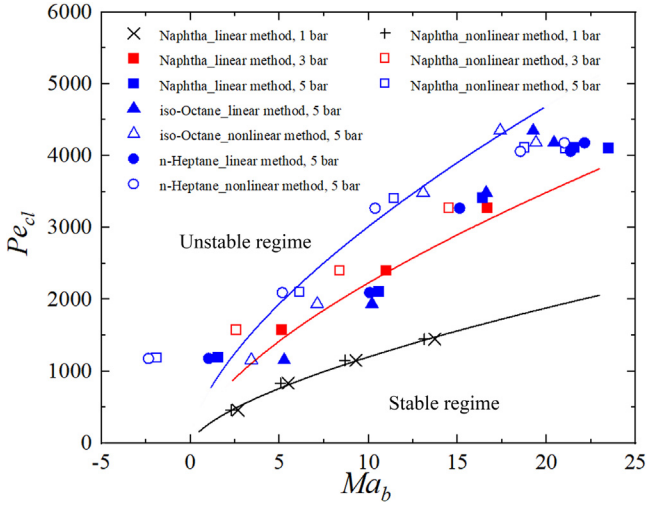

Fig. 12. Variations of Pe_{cl} with respect to Ma_b covering T_i = 360 K and P_i = 1, 3, 5 bar. Three solid lines with the corresponding colors are used to fit the present data points, which splits the Pe_{cl}-Ma_b diagram into two parts representing unstable- and stable- regimes.

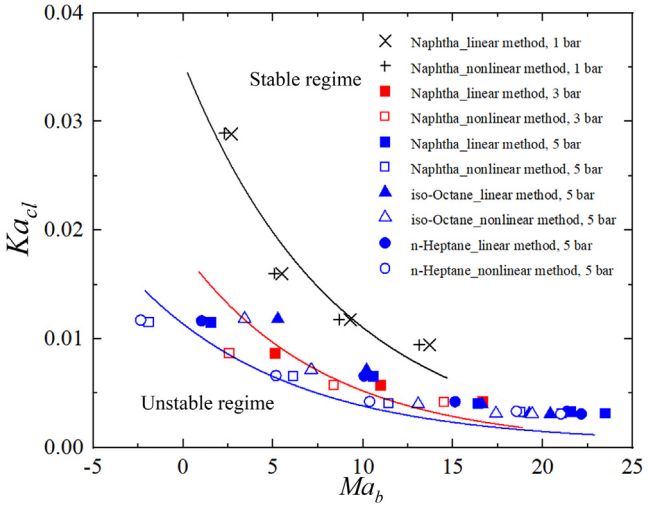

Fig. 13. Variations of Ka_{cl} with respect to Ma_b covering T_i = 360 K and P_i = 1, 3, 5 bar. Three straight solid lines with the corresponding colors are used to fit the present data points, which splits the Ka_{cl}-Ma_b diagram into two parts representing unstable- and stable- regimes.

large-scale unconfined explosions of initially quiet premixed gases, such instabilities can be important [33]. Theoretically, another expression of Markstein number Ma is proposed by [50]:

$$Ma = \frac{\sigma}{\sigma - 1}\ln\sigma + \frac{\hat{\beta}(\mathrm{Le} - 1)}{2(\sigma - 1)}\int_0^{\sigma-1}\frac{\ln(1+x)}{x}dx \tag{12}$$

where $\hat{\beta}$ is Zeldovich number, Le is Lewis number. Due to that DL instability arises from density jump across the flame thickness, the term of density ratio σ relates to the hydrodynamic instability. On the other hand, one of the main components in Eq. (12) for Markstein number is Lewis number. Lewis number describes the competence of thermal diffusivity to mass diffusivity, affecting thermal diffusion instabilities directly. As a result, Markstein number also accounts for thermal diffusion and hydrodynamic effects. Consequently, r_{cl} and L_b are dimensionless into Pe_{cl} and Ma_b to discover the generality of the naphtha-air mixture at a broad variety of beginning circumstances in order to identify the generality of flame DL and TD instability regime.

The associations between Pe_{cl} and Markstein number variations have been shown in [31,33]. Figure 12 depicts the fluctuations of Pe_{cl} in relation to Ma_b at T_i = 360 K and P_i = 1, 3, 5 bar. With an increase in Ma_b, Pe_{cl} values rise. As Ma_b diminishes, the early smooth proclivity of the flame to cellularity increases, and the stable regime is greatly decreased, especially for strongly negative Ma_b. Stretching with a positive Ma_b can help to reduce the inherent hydrodynamic instability. It can also be found that the distributions are quite similar for naphtha, iso-octane and n-heptane-air mixtures at P_i = 5 bar. In addition, the correlation of Pe_{cl} and Ma_b taking the pressure effects into account is represented as:

$$Pe_{cl} = 280\left(Ma_b^{0.64}\right)\left(\frac{P_i}{P_0}\right)^{0.56} R^2 = 0.81 \tag{13}$$

where P_0 is 1 bar. R^2 is the coefficient of determination value. The closer the R^2 value is to 1, the higher the coincidence degree is, and the closer it is to 0, the lower the coincidence degree is.

The critical laminar Karlovitz number, Ka_{cl}, can be considered to be a more relevant parameter evaluating flame instability than Pe_{cl}, described in Section 4. In previous studies, the expressions of Ka_{cl} with Ma_b were used based on exponential equations [31,33]. Similarly, variations of Ka_{cl} with Ma_b at T_i = 360 K, P_i = 1, 3, 5 bar are presented in Fig. 13. The relationship of Ka_{cl} and Ma_b taking the pressure effects into account is expressed as follows:

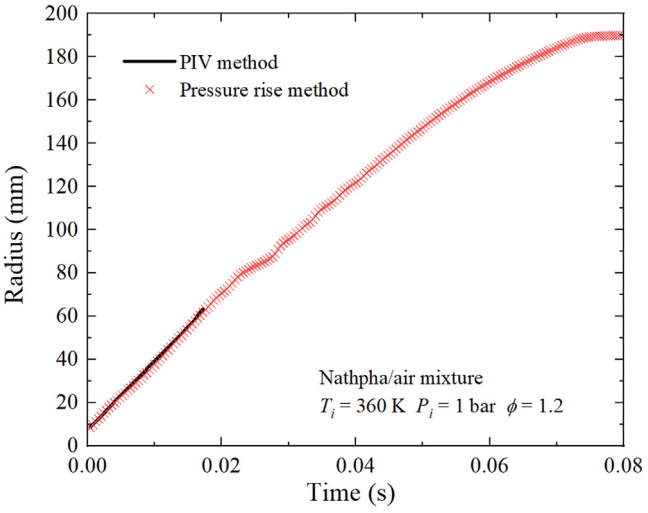

Fig. 14. Mean flame radius for coal-based naphtha-air flames at ϕ = 1.2, T_i = 360 K, P_i = 1 bar.

$$Ka_{cl} = 0.037\left(0.88^{Ma_b}\right)(P_i/P_0)^{-0.65}\, R^2 = 0.7 \tag{14}$$

Figure 14 shows the transient flame radius obtained by the PIV method. The smooth flame radius value obtained from the pressure record (Eq. (7)) is also plotted in Fig. 14 (cross symbol) and is reassuringly consistent with the trends obtained by PIV technique. Further comparison of complete PIV and pressure method statistics is beyond the scope of current work and will be reserved for future investigation. Details of the uncertainty in the extrapolation method are presented in [51]. And it is reported that the relative uncertainties in r_m (Eq. (7)) varied from 17% to 5% from the highest to the lowest propagating speed. The uncertainties in u_{tm} (Eq. (8)) varied from 5% to 21% at the highest and lowest radii for different propagating speeds.

Figure 15 presents the burning velocity for coal-based naphtha-air flames at T_i = 360 K, P_i = 5 bar. The spontaneous increase and strong oscillation of u_{tm} can be found in rich conditions, especially at ϕ = 1.5. Significantly increased net volume creation at reaction rate caused by burning rate acceleration caused by the DL and TD instabilities. After that, an acoustic wave and a rapid

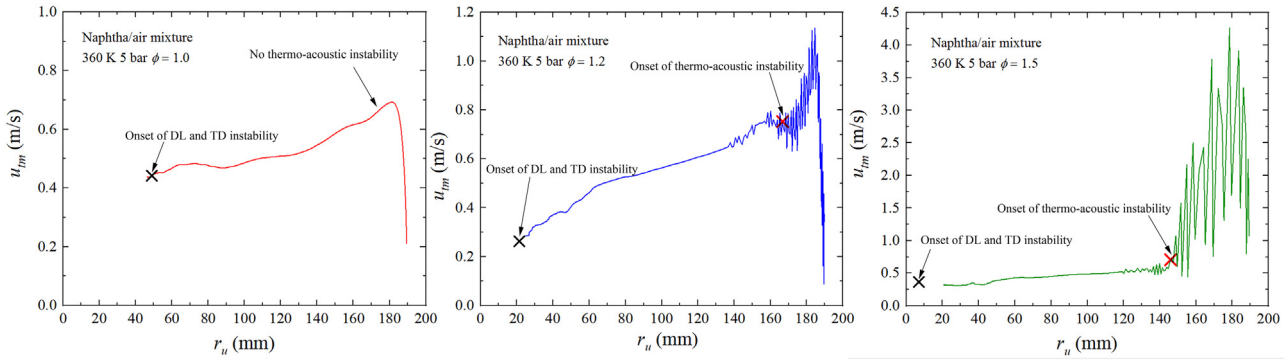

Fig. 15. Burning velocity for coal-based naphtha-air flames at T_i = 360 K, P_i = 5 bar.

change in heat release rate are combined to produce powerful oscillations in pressure and burning velocity. These, in turn, generated thermos-acoustic instability further wrinkled the flame surfaces, and speeded up the burning process. Consequently, the moment satisfying the flame oscillations and burning rate increase is defined as the onset of thermo-acoustic instability (red cross symbol in Fig. 15) in this study, which is much later than the onset of DL and TD instabilities.

On the other hand, at ϕ = 1.0 and lean conditions, there is no obvious evidence of oscillations and thermo-acoustic instability. Such instabilities in high pressure laminar explosions are highly related to Markstein length and number. Low or even negative Markstein length and number, as indicated in Figs. 11-13, cause DL and TD instability to manifest early. Meanwhile, in combination with Fig. 8,Fig. 15 substantiates that low or even negative Markstein length and number also contribute to the early occurrence and severe intensity of thermo-acoustic instability.

Additionally, at a flame radius of 180 mm, when the thermo-acoustic instability is at its worst, u_{tm} almost reaches its maximum value. To quantitatively study the thermos-acoustic instability, making an approximate estimate of the burning velocity, u_{nf}, in the last stage of the explosion (r_u =180 mm) is of importance. Values of u_{nf} of mixtures of coal-based naphtha fuel normalized by the unstretched laminar burning velocity, u_l, are plotted against ϕ in Fig. 16(a) for the quantitative analysis. The values of u_l at ϕ = 1.4, 1.5 for 3 and 5 bar are also derived from the pressure method.

It shows high enhancement ratios of u_{nf}/u_l for the rich mixtures with quite low Markstein numbers and severe pressure oscillations. Al-Shahrany et al. [52] observed a maximum burning velocity enhancement ratio, u_n/u_l, of almost 7 due to thermo-acoustic instabilities with very mild pressure oscillations. Flame wrinkling due to hydrodynamic and thermal diffusion instabilities may have been reinforced by thermo-acoustic instabilities, as evidenced by much larger u_{nf}/u_l ratios of up to almost 16 at ϕ = 1.5 in Fig. 16(a). The u_{nf} /u_l of iso-octane/air mixtures from [36] are also presented in Fig. 16(a) for comparison. Thermo-acoustic instabilities generated by coal-based naphtha-air mixtures are demonstrably less severe than iso-octane/air mixtures, but more severe than n-heptane-air mixtures.

Since the onset of instability has a monotonous increasing or decreasing trend with the effect of stretch, Ma_b. As also shown in Figs. 12 and 13, the stretch affects flame instability significantly. Dimensionless group analysis is performed to gain deeper insight into the phenomena that lead to thermo-acoustic instability as well. The fluctuations of u_{nf} /u_l with respect to Ma_b are shown in Fig. 16(b) to help understand the influence of stretch on the thermo-acoustic instability evolved from DL and TD instability with the acoustic wave. Due to the fact that cellular instability of naphtha-air mixtures at ϕ = 1.4, 1.5 for 3 and 5 bar begins at the very beginning, obtaining Markstein length and number would be difficult and inaccurate. As a result, the relevant situations will not be considered in this study. The results demonstrate that stretch reduces the strength of thermo-acoustic instability, as can be seen by the declining trends. The exponentially fitting equa-

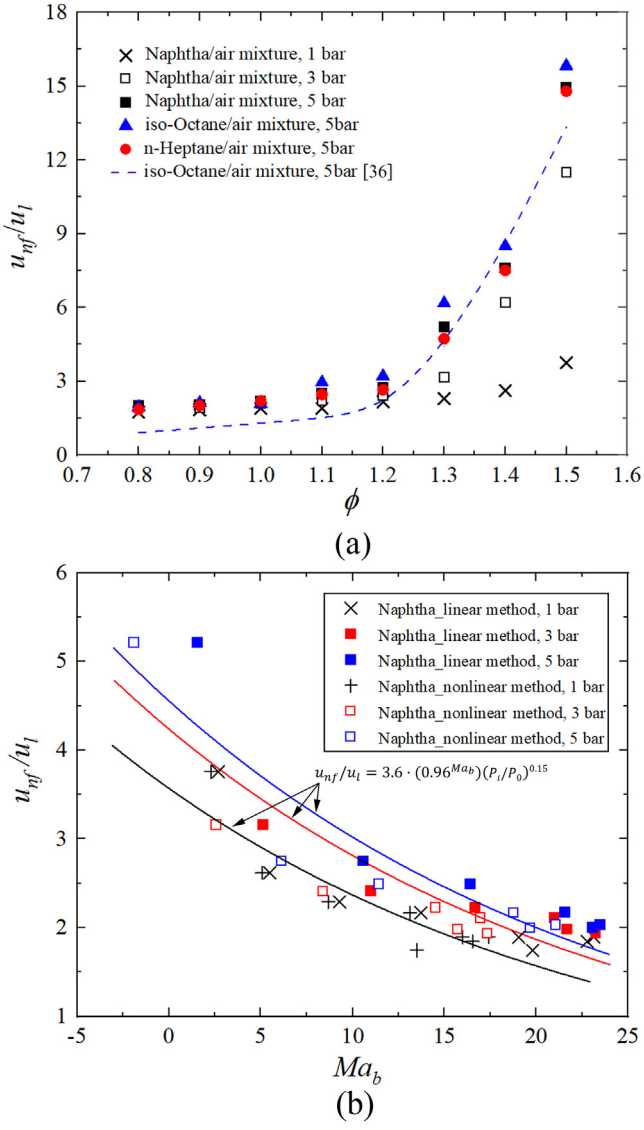

Fig. 16. Normalized maximum burning velocity u_{nf} /u_l plotted against ϕ (a) and u_{nf} /u_l with respect to Ma_b (b) for coal-based naphtha-air mixtures at T_i = 360 K.

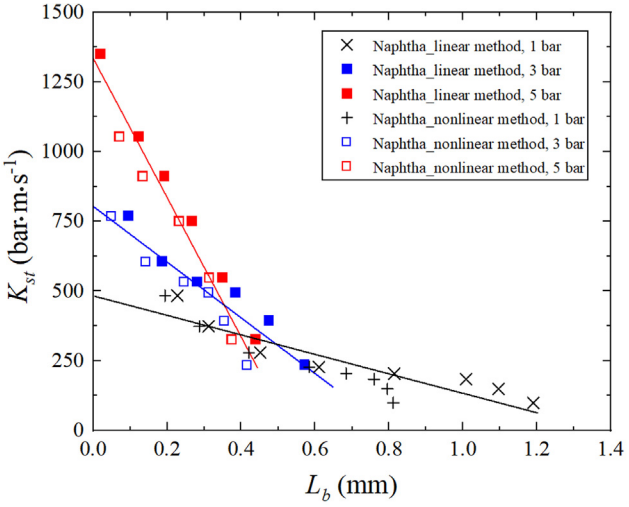

Fig. 17. Variations of K_{st} with respect to L_b covering T_i = 360 K and P_i = 1, 3, 5 bar (a) and dependence of $K_{st,0}$ on the initial pressure (b).

tion is adopted to fit the data:

$$u_{nf}/u_l = 3.6 \cdot \left(0.96^{Ma_b}\right)(P_i/P_0)^{0.15}\, R^2 = 0.78 \tag{15}$$

On the other hand, the thermo-acoustic instability also enhances combustion intensity, as shown in Fig. 4. Variations of K_{st} with respect to Markstein length L_b are shown in Fig. 17. As L_b increases, so does the combustion intensity. The slope between K_{st} and L_b becomes steeper as pressure rises, implying that under high pressure, the stretch effect makes it simpler to lower combustion intensity. This means that lower values of the stretch rate or negative values of Markstein number would be conducive to enhancing the combustion intensity, which further increases the heat release rate and efficiency in combustors. For $K_{st} > 0$, the linear model is adopted to get the unstretched $K_{st,0}$ of K_{st} at Markstein length = 0 mm:

$$K_{st} = K_{st,0} - k_{st}L_b = \begin{cases} 480 - 350L_b, & P_i = 1\ bar \\ 800 - 1000L_b, & P_i = 3\ bar \\ 1350 - 2500L_b, & P_i = 5\ bar \end{cases} \tag{16}$$

Here, $K_{st,0}$ is the unstretched K_{st}, k_{st} is used to characterize the effect of Markstein length on combustion intensity deflagration index, K_{st}. The values of $K_{st,0}$ at 1, 3, 5 bar are 480, 800, 1350 bar-m/s. The dependence of $K_{st,0}$ on the initial pressure is a monotonic dependence, which is easily observable.

6. Conclusions

The detailed compositions of coal-based naphtha have been analysed using the GC-DHA method. A 3-component surrogate fuel has been proposed based on the C/H ratio and RON. This surrogate model was validated against measured values of laminar burning velocities, using PIV technique in a constant volume spherical combustion vessel at an initial temperature of T_i = 360 K and a range of initial pressure up to 5 bar. The pressure traces of coal-based naphtha are between iso-octane and n-heptane. Oscillations of pressure traces were observed in the explosions of the rich mixtures, which can be attributed to the high thermo-acoustic instabilities induced by severe interaction between Darrieus-Landau (hydrodynamic) or thermal diffusion instabilities and acoustic waves. The thermo-acoustic instability generated by coal-based naphtha-air mixtures is more severe, compared with that in iso-octane explosions. To analyse the critical flame instability conditions of the examined fuels, empirical formulas for Pe_{cl} and Ka_{cl} have been obtained. The dimensionless burning velocity u_{nf}/u_l becomes very high, as a result of the high thermo-acoustic instability at the rich condition of naphtha-air mixtures with low Markstein numbers. The relationships of K_{st} and L_b also demonstrate that a lower stretch effect or negative Markstein number is favorable to increasing combustion intensity, hence increasing the heat release rate and efficiency of practical combustors.

Declaration of Competing Interest

The authors declare that they have no known competing financial interests or personal relationships that could have appeared to influence the work reported in this paper.

Acknowledgements

The authors thank EPSRC (Grant No. EP/W002299/1) for the financial support. Mr. Yu Xie acknowledges the China Scholarship Council and University of Leeds for a joint PhD scholarship (CSC202008350141). Mr. An Lu thanks the China Scholarship Council for the financial support of academic visit at University of Leeds (CSC202106567003). Authors thank Shell for conducting the Detailed Hydrocarbon Analysis for the coal-based naphtha, provided to them by University of Leeds.

Supplementary materials

Supplementary material associated with this article can be found, in the online version, at doi:10.1016/j.combustflame.2023.112625.

Appendix A

The theoretical deduction of Eq. (10) is detailed in follows:
The total stretch rate at the cold front of the flame is:

$$\alpha = \frac{1}{A}\frac{dA}{dt} = \frac{2}{r_u}\frac{dr_u}{dt} = \frac{2}{r_u}S_n$$

At the critical point:

$$\alpha_{cl} = 2\frac{(S_s - L_b\alpha_{cl})}{r_{cl}}$$

$$\alpha_{cl}\frac{\delta}{u_l} = 2\frac{1}{r_{cl}}\frac{\delta}{u_l}(S_s - L_b\alpha_{cl})$$

By definition ($Ka_{cl} = \alpha_{cl}\frac{\delta}{u_l}$)[Bradley et al., 2009]

$$Ka_{cl} = \frac{2}{Pe_{cl}}\left(\frac{S_s}{u_l} - \frac{L_b\alpha_{cl}}{u_l}\right)\left(\because Pe_{cl} = \frac{r_{cl}}{\delta}\right)$$

$$Ka_{cl} = \frac{2}{Pe_{cl}}\left(\sigma - \frac{L_b}{u_l}\frac{2S_n}{r_{cl}}\right)$$

$$Ka_{cl} = \frac{2}{Pe_{cl}}\left[\sigma - 2\frac{L_b}{S_s}\sigma\left(\frac{S_s - L_b\alpha_{cl}}{\frac{r_{cl}}{\delta}\delta}\right)\right]$$

$$Ka_{cl} = \frac{2\sigma}{Pe_{cl}}\left[1 - 2\frac{L_b}{\delta}\left(\frac{S_s - L_b\alpha_{cl}}{S_s\frac{r_{cl}}{\delta}\delta}\right)\right]$$

$$Ka_{cl} = \frac{2\sigma}{Pe_{cl}}\left[1 - \frac{2Ma_b}{Pe_{cl}}\left(\frac{S_s}{S_s} - \frac{L_b\alpha_{cl}}{S_s}\right)\right]$$

$$Ka_{cl} = \frac{2\sigma}{Pe_{cl}}\left[1 - \frac{2Ma_b}{Pe_{cl}} + \frac{2Ma_b}{Pe_{cl}}\frac{L_b\alpha_{cl}}{S_s}\right]$$

$$Ka_{cl} = \frac{2\sigma}{Pe_{cl}}\left[1 - \frac{2Ma_b}{Pe_{cl}} + \frac{2Ma_b}{Pe_{cl}}L_b\frac{2S_n}{r_{cl}}\frac{1}{S_s}\right]\left(\because \alpha_{cl} = \frac{2S_n}{r_{cl}}\right)$$

$$Ka_{cl} = \frac{2\sigma}{Pe_{cl}}\left[1 - \frac{2Ma_b}{Pe_{cl}} + \frac{2Ma_b}{Pe_{cl}}\frac{L_b}{S_s}\frac{2(S_s - L_b\alpha_{cl})}{r_{cl}/S_s}\frac{1}{S_s}\right](\because S_n = S_s - L_b\alpha)$$

$$Ka_{cl} = \frac{2\sigma}{Pe_{cl}}\left[1 - \frac{2Ma_b}{Pe_{cl}} + \frac{2Ma_b}{Pe_{cl}}\frac{2Ma_b}{Pe_{cl}}\left(\frac{S_s}{S_s} - \frac{L_b\alpha_{cl}}{S_s}\right)\right]$$

$$Ka_{cl} = \frac{2\sigma}{Pe_{cl}}\left[1 - \frac{2Ma_b}{Pe_{cl}} + \left(\frac{2Ma_b}{Pe_{cl}}\right)^2\left\{1 - \frac{L_b}{S_s}\frac{2(S_s - L_b\alpha_{cl})}{r_{cl}/S_s}\frac{1}{S_s}\right\}\right]$$

$$Ka_{cl} = \frac{2\sigma}{Pe_{cl}}\left[1 - \frac{2Ma_b}{Pe_{cl}} + \left(\frac{2Ma_b}{Pe_{cl}}\right)^2 - \left(\frac{2Ma_b}{Pe_{cl}}\right)^3\left\{\frac{S_s}{S_s} - \frac{L_b\alpha_{cl}}{S_s}\right\}\right]$$

Similar to $(1 - x + x^2 - x^3 + \ldots.) = (1 + x)^{-1}$ Binomial expansion

Therefore, $Ka_{cl} = \frac{2\sigma}{Pe_{cl}}[1 + \frac{2Ma_b}{Pe_{cl}}]^{-1}$

References

[1] A. Calam, B. Aydoğan, S. Halis, The comparison of combustion, engine performance and emission characteristics of ethanol, methanol, fusel oil, butanol, isopropanol and naphtha with n-heptane blends on HCCI engine, Fuel 266 (2020) 117071.

[2] S. Çelebi, B. Duzcan, U. Demir, A. Uyumaz, C. Haşimoglu, Effects of light naphtha utilization on engine performance in an homogeneous charged compression ignition engine, Fuel 306 (2021) 121663.

[3] M. Höök, K. Aleklett, A review on coal-to-liquid fuels and its coal consumption, Int. J. Energy Res. 34 (10) (2010) 848–864.

[4] A. Lu, C. Zhang, Y. Ren, Y. Li, S. Li, P. Yin, Research on knock recognition of coal-based naphtha homogeneous charge compression ignition engine based on combined feature extraction and classification, Fuel 300 (2021) 120997.

[5] P. Jaramillo, W.M. Griffin, H.S. Matthews, Comparative analysis of the production costs and life-cycle GHG emissions of FT liquid fuels from coal and natural gas, Environ. Sci. Technol. 42 (2008) 7559–7565.

[6] Y. Shen, S. Shuai, J. Wang, J. Xiao, Optimization of gasoline hydrocarbon compositions for reducing exhaust emissions, J. Environ. Sci. 21 (2009) 1208–1213.

[7] A.M. Hochhauser, Review of prior studies of fuel effects on vehicle emissions, SAE Int. J. Fuels Lubr. 2 (2009) 541–567.

[8] R. Perry, I.L. Gee, Vehicle emissions in relation to fuel composition, Sci. Total Environ. 169 (1995) 149–156.

[9] F. Ouyang, X. Pei, X. Zhao, H. Weng, Effect of operation conditions on the composition and octane number of gasoline in the process of reducing the content of olefins in fluid catalytic cracking (FCC) gasoline, Energy Fuels 24 (2010) 475–482.

[10] Y. Kim, Y. Kim, J. Kang, S. Jun, S. Rew, D. Lee, S. Park, Fuel effect on particle emissions of a direct injection engine, SAE Tech. Pap. Ser. 2 (2013).

[11] K. Saitoh, M. Hamasaki, Effects of sulfur, aromatice, T50, T90 and MTBE on mass exhaust emissions from vehicles with advanced technology-JCAP gasoline WG STEP II report, SAE Trans. (2003) 1700–1718.

[12] Y. Sogawa, H. Hattori, N. Yanagisawa, M. Hosoya, T. Shoji, Y. Iwakiri, T. Yamashita, T. Ikeda, S. Tanaka, K. Takahashi, T. Suzuki, T. Nakajima, Y. Tonegawa, Nano particle emission evaluation of state of the art diesel aftertreatment technologies (DPF, urea-SCR and DOC), gasoline combustion systems (Lean Burn/Stoichiometric DISI and MPI) and fuel qualities effects (EtOH, ETBE, FAME, Aromatics and Distillation), SAE Trans. (2007) 1013–1023.

[13] C.L. Goodfellow, Jr.R.A. Gorse, M.J. Hawkins, J.S. McArragher, European programme on emissions, fuels and engine technologies (EPEFE)-gasoline aromatics/E100 study, SAE Trans. (1996) 503–526.

[14] A.M. Hochhauser, J.D. Benson, R.A. Gorse jr, W.J. Koehl, L.J. Painter, B.H. Rippon, R.M. Reuter, J.A. Rutherford, The Effect of aromatics, MTBE, olefins and T_{9n} on mass exhaust emissions from current and older vehicles-The auto/oil air quality improvement research program, SAE Trans. (1991) 748–788.

[15] A. Ahmed, M. Khurshid, N. Naser, B. Jihad, G. Pattrick, H.C. Suk, L.R. William, S. Mani, Surrogate fuel formulation for light naphtha combustion in advanced combustion engines, 7th European Combustion Meeting, Budapest (2015).

[16] D. Mitakos, C. Blomberg, A. Vandersickel, Y. Wright, B. Schneider, K. Boulouchos, Ignition delays of different homogeneous fuel-air mixtures in a rapid compression expansion machine and comparison with a 3-stage-ignition model parameterized on shock tube data, SAE Int. J. Engines 6 (4) (2013) 1934–1952.

[17] M. Alabbad, G. Issayev, B. Jihad, K.V. Alexander, R.G. Binod, D. Khalil, A. Ahfaz, S. Mani, F. Aamir, Autoignition of straight-run naphtha: a promising fuel for advanced compression ignition engines, Combust. Flame 189 (2018) 337–346.

[18] A. Zhong, X. Li, T. Turányi, Z. Huang, D. Han, Pyrolysis and oxidation of a light naphtha fuel and its surrogate blend, Combust. Flame 240 (2022) 111979.

[19] Y. Dong, C.M. Vagelopoulos, G.R. Spedding, F.N. Egolfopoulos, Measurement of laminar flame speeds through digital particle image velocimetry: mixtures of methane and ethane with hydrogen, oxygen, nitrogen, and helium, Proc. Combust. Inst. 29 (2) (2002) 1419–1426.

[20] S. Balusamy, A. Cessou, B. Lecordier, Direct measurement of local instantaneous laminar burning velocity by a new PIV algorithm, Exp. Fluids 50 (4) (2011) 1109–1121.

[21] E. Varea, V. Modica, A. Vandel, B. Renou, Measurement of laminar burning velocity and Markstein length relative to fresh gases using a new postprocessing procedure: application to laminar spherical flames for methane, ethanol and isooctane/air mixtures, Combust. Flame 159 (2) (2012) 577–590.

[22] D. Bradley, M. Lawes, M.E. Morsy, Flame speed and particle image velocimetry measurements of laminar burning velocities and Markstein numbers of some hydrocarbons, Fuel 243 (2019) 423–432.

[23] V. Knop, M. Loos, C. Pera, N. Jeuland, A linear-by-mole blending rule for octane numbers of n-heptane/iso-octane/toluene mixtures, Fuel 115 (2014) 666–673.

[24] M. Mehl, W.J. Pitz, C.K. Westbrook, H.J. Curran, Kinetic modeling of gasoline surrogate components and mixtures under engine conditions, Proc. Combust. Inst. 33 (1) (2011) 193–200.

[25] Y. Xie, J. Li, J. Yang, R. Cracknell, Laminar burning velocity blending laws using particle imaging velocimetry, Appl. Energy Combust. Sci. 13 (2023) 100114.

[26] DantecDantec Dynamic Studio, 2015 https://www.dantecdynamics.com/.

[27] D. Bradley, G. Roth, Adaptive thresholding using the integral image, J. Graph. Tools 12 (2) (2007) 13–21.

[28] A.P. Kelley, C.K. Law, Nonlinear effects in the extraction of laminar flame speeds from expanding spherical flames, Combust. Flame 156 (9) (2009) 1844–1851.

[29] Z. Chen, On the extraction of laminar flame speed and Markstein length from outwardly propagating spherical flames, Combust. Flame 158 (2) (2011) 291–300.

[30] F. Halter, T. Tahtouh, C. Mounaïm-Rousselle, Nonlinear effects of stretch on the flame front propagation, Combust. Flame 157 (2010) 1825–1832.

[31] Y. Xie, M.E. Morsy, J. Li, J. Yang, Intrinsic cellular instabilities of hydrogen laminar outwardly propagating spherical flames, Fuel 327 (2022) 125149.

[32] D. Bradley, M. Lawes, M.S. Mansour, Correlation of turbulent burning velocities of ethanol–air, measured in a fan-stirred bomb up to 1.2MPa, Combust. Flame 158 (1) (2011) 123–138.

[33] M.E. Morsy, J. Yang, The instability of laminar methane/hydrogen/air flames: correlation between small and large-scale explosions, Int. J. Hydrog. Energy 47 (69) (2022) 29959–29970.

[34] P. Clavin, Dynamic behavior of premixed flame fronts in laminar and turbulent flows, Prog. Energy Combust. Sci. 11 (1) (1985) 1–59.

[35] C. Morley, GASEQ: A Chemical Equilibrium Program for Windows, 2005 http://www.gaseq.co.uk.

[36] A.S. Al-Shahrany, D. Bradley, M. Lawes, K. Liu, R. Woolley, Darrieus–Landau and thermo-acoustic instabilities in closed vessel explosions, Combust. Sci. Technol. 178 (10–11) (2006) 1771–1802.

[37] J. Goulier, N. Chaumeix, F. Halter, N. Meynet, A. Bentaïb, Experimental study of laminar and turbulent flame speed of a spherical flame in a fan-stirred closed vessel for hydrogen safety application, Nucl. Eng. Des. 312 (2017) 214–227.

[38] R.D. Mumby, Experimental Characterisation of Fuel Blends (Doctoral dissertation, University of Leeds, 2016.

[39] W. Liang, F. Wu, C.K. Law, Extrapolation of laminar flame speeds from stretched flames: role of finite flame thickness, Proc. Combust. Inst. 36 (1) (2017) 1137–1143.

[40] F. Wu, W. Liang, Z. Chen, Y. Ju, C.K. Law, Uncertainty in stretch extrapolation of laminar flame speed from expanding spherical flames, Proc. Combust. Inst. 35 (1) (2015) 663–670.

[41] O. Mannaa, M.S. Mansour, W.L. Roberts, S.H. Chung, Laminar burning velocities at elevated pressures for gasoline and gasoline surrogates associated with RON, Combust. Flame 162 (6) (2015) 2311–2321.

[42] C.K. Law, Combustion Physics, Cambridge University Press, New York, USA. (2006), pp. 89–96.

[43] M. Lawes, G.J. Sharpe, N. Tripathi, R.F. Cracknell, Influence of spark ignition in the determination of Markstein lengths using spherically expanding flames, Fuel 186 (2016) 579–586.

[44] M.P. Burke, Z. Chen, Y. Ju, F.L. Dryer, Effect of cylindrical confinement on the determination of laminar flame speeds using outwardly propagating flames, Combust. Flame 156 (4) (2009) 771–779.

[45] Z. Chen, M.P. Burke, Y. Ju, Effects of compression and stretch on the determination of laminar flame speeds using propagating spherical flames, Combust. Theor. Model. 13 (2) (2009) 343–364.

[46] Z. Chen, Effects of radiation and compression on propagating spherical flames of methane/air mixtures near the lean flammability limit, Combust. Flame 157 (12) (2010) 2267–2276.

[47] ANSYS Reaction DesignChemkin Pro 19.2, San Diego, 2019.

[48] M. Mehl, J.Y. Chen, W.J. Pitz, S.M. Sarathy, C.K. Westbrook, An approach for formulating surrogates for gasoline with application toward a reduced surrogate mechanism for CFD engine modeling, Energy Fuels 25 (11) (2011) 5215–5223.

[49] S.G. Davis, C.K. Law, Laminar flame speeds and oxidation kinetics of iso-octane-air and n-heptane-air flames, Symp. (Int.) Combust. 27 (1) (1998) 521–527.

[50] J.K. Bechtold, M. Matalon, Hydrodynamic and diffusion effects on the stability of spherically expanding flames, Combust. Flame 67 (1) (1987) 77–90.

[51] P. Ahmed, B. Thorne, M. Lawes, S. Hochgreb, G.V. Nivarti, R.S. Cant, Three dimensional measurements of surface areas and burning velocities of turbulent spherical flames, Combust. Flame 233 (2021) 111586.

[52] A.S. Al-Shahrany, D. Bradley, M. Lawes, R. Woolley, Measurement of unstable burning velocities of iso-octane-air mixtures at high pressure and the derivation of laminar burning velocities, Proc. Combust. Inst. 30 (1) (2005) 225–232.